PERGAMON

International Journal of Heat and Mass Transfer 44 (2001) 3253–3264

International Journal of HEAT and MASS TRANSFER

www.elsevier.com/locate/ijhmt

Elliptic temperature contours under a transverse magnetic field computed for a Czochralski melt

Masato Akamatsu [a], Mitsuo Higano [a], Hiroyuki Ozoe [b,*]

[a] *Department of Machine Intelligence and Systems Engineering, Akita Prefectural University, 84-4 Tsuchiya-Ebinokuchi, Honjo, Akita 015-0055, Japan*

[b] *Institute of Advanced Material Study, Kyushu University, Kasuga Koen 6-1, Kasuga 816-8580, Japan*

Received 7 July 2000; received in revised form 13 October 2000

Abstract

The melt flow in a Czochralski system with radiative cooling from the melt surface under a horizontal magnetic field was studied by transient three-dimensional numerical computation. A quite peculiar convection mode was obtained under the present magnetic field. Velocity components were all downwards in a vertical cross-section parallel to the magnetic field, while those in a plane perpendicular to the magnetic field were natural convection dominant. A top view of temperature contours represented an elliptic shape which was supported by a practically grown crystal rod with an elliptic cross-section.

Keywords: Czochralski method; Transverse magnetic field; Numerical computation; Natural convection; Forced convection

1. Introduction

The silicon single crystals are mainly manufactured by Czochralski crystal growing methods. The wafers of the silicon single crystals are used for the basis of the integrated circuits. From a productive viewpoint, productions of the silicon single crystals with the large diameter are required at present. The convectional control in a Czochralski crucible is one of the most important subjects to obtain a high quality crystal. However, it is difficult to control thermal convection in a crucible with the large diameter only by the rotation of a crucible and a crystal. One way of the convection control is the application of the magnetic field, since the melt in a crucible for a Czochralski crystal growing system has high electric conductivity. The electric currents are produced when the melt with high electric conductivity is moving under a magnetic field, and the electric currents interact with a magnetic field to generate Lorentz force. This force can modify the convection of the melt such as the melt of silicon during single crystal growth. Therefore, it is considered that the application of the magnetic field is the important technology for single crystal growth with large diameter in the future. Followings are some recent works related to this application.

The effect of vertical, horizontal magnetic fields for a Czochralski crystal growing system is investigated experimentally [1–5]. The suppression of thermal fluctuation in the melt is reported by the application of an external magnetic field. The effects of axial and transverse magnetic fields on the Czochralski crystal growth were studied theoretically in terms of a simple model by Kobayashi [6]. Yi et al. [7] reported the influence of a vertical magnetic field on the velocity in molten silicon theoretically and experimentally. They measured velocity in the melt by X-ray radiography and clarified the tendency of the velocity by experimental measurement and numerical calculation. The melt flow and oxygen transfer during crystal growth under a magnetic field are investigated numerically [8–11]. The research of the oxygen transfer in the Czochralski melt is important like that of the thermal convection. The effects of the various external magnetic fields have been reported numerically and experimentally for a Czochralski crystal growing

* Corresponding author. Tel.: +81-92-583-7834; fax: +81-92-583-7838.

E-mail address: ozoe@cm.kyushu-u.ac.jp (H. Ozoe).

0017-9310/01/$ - see front matter
PII: S0017-9310(00)00367-7

Nomenclature

b	uniform magnetic flux density (T)
B	dimensionless magnetic flux density vector (dimensionless)
C_p	specific heat of melt (J/(kg K))
E	dimensionless electric field vector (dimensionless)
e	intensity of electric field (V/m)
F	dimensionless Lorentz force vector (dimensionless)
f	Lorentz force (N/m^3)
G	geometrical factor (dimensionless)
g	acceleration due to gravity (m/s^2)
H	dimensionless height of melt in a crucible (dimensionless)
h	height of melt in a crucible (m)
Ha	Hartmann number (dimensionless)
J	dimensionless electric current density vector (dimensionless)
j	electric current density (A/m^2)
Nu	Nusselt number (dimensionless)
Pr	Prandtl number (dimensionless)
P	dimensionless pressure (dimensionless)
p	pressure (Pa)
Q	heat loss (W/m^2)
Ra	Rayleigh number (dimensionless)
Re	rotational Reynolds number (dimensionless)
R	dimensionless radial coordinate (dimensionless)
r	radial coordinate (m)
S	Stefan–Boltzmann constant ($W/(m^2\ K^4)$)
T	dimensionless temperature (dimensionless)
t	time (s)
U	dimensionless velocity vector (dimensionless)
u	velocity component in the radial direction (m/s)
v	velocity component in the circumferential direction (m/s)
w	velocity component in the axial direction (m/s)
Z	dimensionless axial coordinate (dimensionless)
z	axial coordinate (m)

Subscripts

c	cold wall
cond	conductive heat transfer
conv	convective heat transfer
cru	crucible
cry	crystal rod
h	hot wall
R	radial component
Z	axial component
ϕ	circumferential component
0	reference value for dimensionless variable
1	melt
2	furnace

Greek symbols

α	thermal diffusivity of melt (m^2/s)
β	volumetric coefficient of expansion (K^{-1})
ε	emissivity (dimensionless)
η	dimensionless temperature gradient at the melt surface (dimensionless)
θ	temperature (K)
λ	thermal conductivity of melt (W/(m K))
μ	viscosity of melt (Pa s)
ν	kinematic viscosity of melt (m^2/s)
ρ	density of melt (kg/m^3)
σ	electric conductivity of melt ($\Omega^{-1}\ m^{-1}$)
τ	dimensionless time (dimensionless)
ϕ	circumferential coordinate (rad)
Ψ	dimensionless electric scalar potential (dimensionless)
ψ	electric scalar potential (V)
Ω	dimensionless angular velocity (dimensionless)
ω	angular velocity (rad/s)

system. However, the effect of Lorentz force to control the convection has been sought only by a trial and error basis. In the present paper, the works of Lorentz force could be well understood with the detailed information on the electrical fields.

The purpose of this paper is to clarify them in order to understand detailed characteristics under a horizontal magnetic field for a crystal growing system by using the fully three-dimensional numerical calculation.

2. Model system

Fig. 1(a) and (b) shows two model systems of the present calculation with different crystal diameters both subject to uniform horizontal magnetic field. These modeled systems consist of a crucible, melt and a crystal rod. The diameter of a crystal rod for model 1 is 0.5 times that of a crucible. On the other hand, the diameter of a crystal rod for model 2 is 0.08 times that of a crucible. A uniform horizontal magnetic field is impressed in the direction from $\phi = \pi$ to $\phi = 0$. A liquid metal whose Prandtl number is 0.0374 was assumed to fill the crucible. Out going heat flux was imposed on the surface of the melt, since radiative heat transfer becomes dominant at the top of melt due to high temperature. The crystal rod is assumed to be static. The model equations consist of the equation of continuity (Eq. (1)), the momentum equations with the Lorentz force term in the radial (Eq. (2)), in the cir-

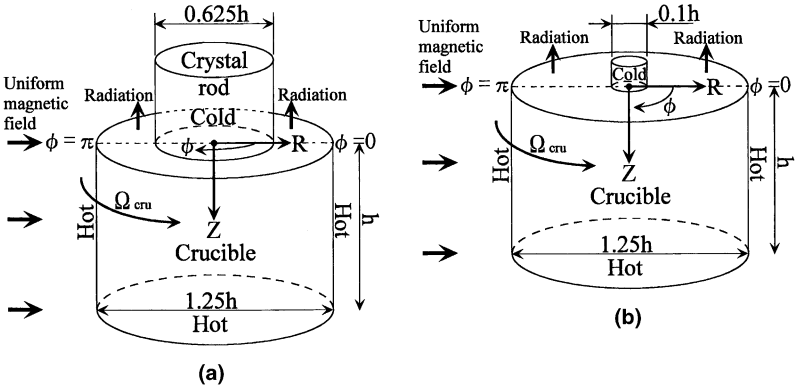

Fig. 1. Two model systems of the present calculation with different crystal diameters both subject to uniform horizontal magnetic field: (a) model 1 with a large crystal rod at the top; (b) model 2 with a small crystal rod at the top.

cumferential (Eq. (3)) and in the axial direction (Eq. (4)) and the energy equation (Eq. (5)) and conservation of electric current density (Eq. (6)) and Ohm's law (Eq. (7)). They are as follows with dimensionless variables.

Equation of continuity

$$\frac{1}{R}\frac{\partial}{\partial R}(RU)+\frac{1}{R}\frac{\partial V}{\partial \phi}+\frac{\partial W}{\partial Z}=0. \tag{1}$$

Momentum equation

$$\begin{aligned}&\frac{\partial U}{\partial \tau}+U\frac{\partial U}{\partial R}+\frac{V}{R}\frac{\partial U}{\partial \phi}+W\frac{\partial U}{\partial Z}-\frac{V^2}{R}\\&\quad=-\frac{\partial P}{\partial R}+Pr\left[\frac{\partial}{\partial R}\left\{\frac{1}{R}\frac{\partial}{\partial R}(RU)\right\}+\frac{1}{R^2}\frac{\partial^2 U}{\partial \phi^2}+\frac{\partial^2 U}{\partial Z^2}\right.\\&\qquad\left.-\frac{2}{R^2}\frac{\partial V}{\partial \phi}\right]+F_R.\end{aligned} \tag{2}$$

$$\begin{aligned}&\frac{\partial V}{\partial \tau}+U\frac{\partial V}{\partial R}+\frac{V}{R}\frac{\partial V}{\partial \phi}+W\frac{\partial V}{\partial Z}+\frac{UV}{R}\\&\quad=-\frac{1}{R}\frac{\partial P}{\partial \phi}+Pr\left[\frac{\partial}{\partial R}\left\{\frac{1}{R}\frac{\partial}{\partial R}(RV)\right\}+\frac{1}{R^2}\frac{\partial^2 V}{\partial \phi^2}\right.\\&\qquad\left.+\frac{\partial^2 V}{\partial Z^2}+\frac{2}{R^2}\frac{\partial U}{\partial \phi}\right]+F_\phi,\end{aligned} \tag{3}$$

$$\begin{aligned}&\frac{\partial W}{\partial \tau}+U\frac{\partial W}{\partial R}+\frac{V}{R}\frac{\partial W}{\partial \phi}+W\frac{\partial W}{\partial Z}\\&\quad=-\frac{\partial P}{\partial Z}-PrT+Pr\left[\frac{1}{R}\frac{\partial}{\partial R}\left\{R\frac{\partial W}{\partial R}\right\}+\frac{1}{R^2}\frac{\partial^2 W}{\partial \phi^2}\right.\\&\qquad\left.+\frac{\partial^2 W}{\partial Z^2}\right]+F_Z.\end{aligned} \tag{4}$$

Energy equation

$$\begin{aligned}&\frac{\partial T}{\partial \tau}+U\frac{\partial T}{\partial R}+\frac{V}{R}\frac{\partial T}{\partial \phi}+W\frac{\partial T}{\partial Z}\\&\quad=\frac{1}{R}\frac{\partial}{\partial R}\left\{R\frac{\partial T}{\partial R}\right\}+\frac{1}{R^2}\frac{\partial^2 T}{\partial \phi^2}+\frac{\partial^2 T}{\partial Z^2}.\end{aligned} \tag{5}$$

Conservation of electric current density

$$\frac{1}{R}\frac{\partial}{\partial R}(RJ_R)+\frac{1}{R}\frac{\partial J_\phi}{\partial \phi}+\frac{\partial J_Z}{\partial Z}=0 \tag{6}$$

Ohm's law

$$\mathbf{J}=\mathbf{E}+\mathbf{U}\times\mathbf{B}=\begin{pmatrix}-\frac{\partial \Psi}{\partial R}-WB_\phi\\-\frac{1}{R}\frac{\partial \Psi}{\partial \phi}+WB_R\\-\frac{\partial \Psi}{\partial Z}+UB_\phi-VB_R\end{pmatrix} \tag{7}$$

Transverse magnetic field

$$\mathbf{B}=\begin{pmatrix}B_R\\B_\phi\\B_Z\end{pmatrix}=\begin{pmatrix}\cos\phi\\-\sin\phi\\0\end{pmatrix} \tag{8}$$

Induced electromotive force

$$\mathbf{U}\times\mathbf{B}=\begin{pmatrix}-WB_\phi\\WB_R\\UB_\phi-VB_R\end{pmatrix} \tag{9}$$

Lorentz force

$$\mathbf{F}=\begin{pmatrix}F_R\\F_\phi\\F_Z\end{pmatrix}=\mathbf{J}\times\mathbf{B}=Ha^2Ra^{-2/3}Pr\begin{pmatrix}-J_ZB_\phi\\J_ZB_R\\J_RB_\phi-J_\phi B_R\end{pmatrix} \tag{10}$$

Following dimensionless variables and reference values were employed in the above equations:

$$R=\frac{r}{r_0},\quad Z=\frac{z}{r_0},\quad \tau=\frac{t}{t_0},\quad U=\frac{u}{u_0},\quad V=\frac{v}{u_0},$$

$$W=\frac{w}{u_0},\quad P=\frac{p}{p_0},\quad \Omega=\frac{\omega}{\omega_0},\quad T=\frac{\theta-\theta_0}{\theta_h-\theta_c},$$

$$H=\frac{h}{r_0},\quad J_R=\frac{j_R}{j_0},\quad J_\phi=\frac{j_\phi}{j_0},\quad J_Z=\frac{j_Z}{j_0},$$
$$B_R=\frac{b_R}{b_0},\quad B_\phi=\frac{b_\phi}{b_0},\quad B_Z=\frac{b_Z}{b_0},\quad E_R=\frac{e_R}{e_0},$$
$$E_\phi=\frac{e_\phi}{e_0},\quad E_Z=\frac{e_Z}{e_0},\quad F_R=\frac{f_R}{f_0},\quad F_\phi=\frac{f_\phi}{f_0},$$
$$F_Z=\frac{f_Z}{f_0},\quad \Psi=\frac{\psi}{\psi_0},\quad Ra=\frac{g\beta(\theta_h-\theta_c)h^3}{\alpha\nu},$$
$$Pr=\frac{\nu}{\alpha},\quad Ha=b_0h\sqrt{\frac{\sigma}{\rho\nu}},\quad Re=\frac{h^2\omega}{\nu},$$
$$r_0=h\cdot Ra^{-1/3},\quad u_0=\frac{\alpha}{r_0},\quad \omega_0=\frac{\alpha}{r_0^2},$$
$$\theta_0=\frac{\theta_h+\theta_c}{2},\quad p_0=\rho u_0^2,\quad e_0=u_0b_0,\quad \psi_0=\alpha b_0,$$
$$t_0=\frac{r_0}{u_0},\quad j_0=\sigma u_0b_0,\quad f_0=\frac{\rho u_0^2}{r_0}$$

Initial and boundary conditions are given as follows for two model systems with different crystal diameters. The crucible is heated from the sidewall and the bottom isothermally. On the other hand, the crystal rod is cooled isothermally. All the boundaries are electrically insulated.

Initial conditions are:

$$T=0,\quad U=V=W=0,\quad J_R=J_\phi=J_Z=0,\quad \Psi=0.$$

Boundary conditions are:

at $R=0.625H$ and $0\leqq Z\leqq fH$:

$$T=0.5,\quad U=W=0,\quad V=R\Omega_{cru},\quad J_R=0,\quad \frac{\partial\Psi}{\partial R}=0,$$

at $0\leqq R\leqq 0.625H$ and $Z=H$:

$$T=0.5,\quad U=W=0,\quad V=R\Omega_{cru},$$
$$J_Z=0,\quad \frac{\partial\Psi}{\partial Z}=-VB_R,$$

at $0\leqq R\leqq 0.3125H$ or $0\leqq R\leqq 0.05H$ and $Z=0$:

$$T=-0.5,\quad U=V=W=0,\quad J_Z=0,\quad \frac{\partial\Psi}{\partial Z}=0,$$

at $0.3125H<R<0.625H$ or $0.05H<R<0.625H$ and $Z=0$:

$$\frac{\partial T}{\partial Z}=\eta,\quad \frac{\partial U}{\partial Z}=\frac{\partial V}{\partial Z}=0,\quad W=0,\quad J_Z=0,$$
$$\frac{\partial\Psi}{\partial Z}=UB_\phi-VB_R.$$

Heat loss from the melt surface was assumed to be given as follows:

$$\left(\frac{\partial T}{\partial Z}\right)_{Z=0}=\eta=\frac{QRa^{-1/3}}{\lambda(\theta_h-\theta_c)/h},\quad Q=S\varepsilon_1\varepsilon_2(\theta_1^4-\theta_2^4)G_{12} \tag{11}$$

Here, Q, S, ε_1, ε_2, θ_1, θ_2 and G_{12} are the heat loss from the melt surface, Stefan–Boltzmann constant, emissivity of the melt, emissivity of the furnace, melting point of the melt, temperature of the furnace and geometrical factor, respectively. Dimensionless temperature gradient

Table 1
Physical properties of InSb melt and furnace [15,16]

ρ (kg/m^3)	6.48×10^3
β (K^{-1})	9.81×10^{-5}
μ (kg/(m s))	2.34×10^{-3}
λ (W/(m K))	17.7
ν (m^2/s)	3.61×10^{-7}
α (m^2/s)	9.65×10^{-6}
C_p (J/(kg K))	0.283×10^3
σ (Ω^{-1} m^{-1})	0.95×10^6
ε_1 (dimensionless)	0.30
θ_1 (K)	798
S (W/(m^2 K^4))	5.669×10^{-8}
ε_2 (dimensionless)	0.35
θ_2 (K)	300
G_{12} (dimensionless)	1

Table 3
Dimensional equivalence values

h (m)	0.04
r_0 (m)	6.84×10^{-4}
u_0 (m/s)	1.41×10^{-2}
ω_0 (s^{-1})	20.6
t_0 (s)	0.048
$\theta_h-\theta_c$ (°C)	11.32
b_0 (T)	0.124 ($Ha=100$)
p_0 (Pa)	1.29
e_0 (V/m)	1.75×10^{-3}
ψ_0 (V)	1.20×10^{-6}
j_0 (A/m^2)	1.66×10^{-3}
f_0 (N/m^3)	1.88×10^{-3}

Table 2
Numerical conditions

Type	Model	Ha (dimensionless)	Ra (dimensionless)	Pr (dimensionless)	Re_{cry} (dimensionless)	Re_{cru} (dimensionless)	η (dimensionless)
A	1	100	2×10^5	0.0374	0	−362	8.09×10^{-3}
B		200					
C		300					
D	2	200					

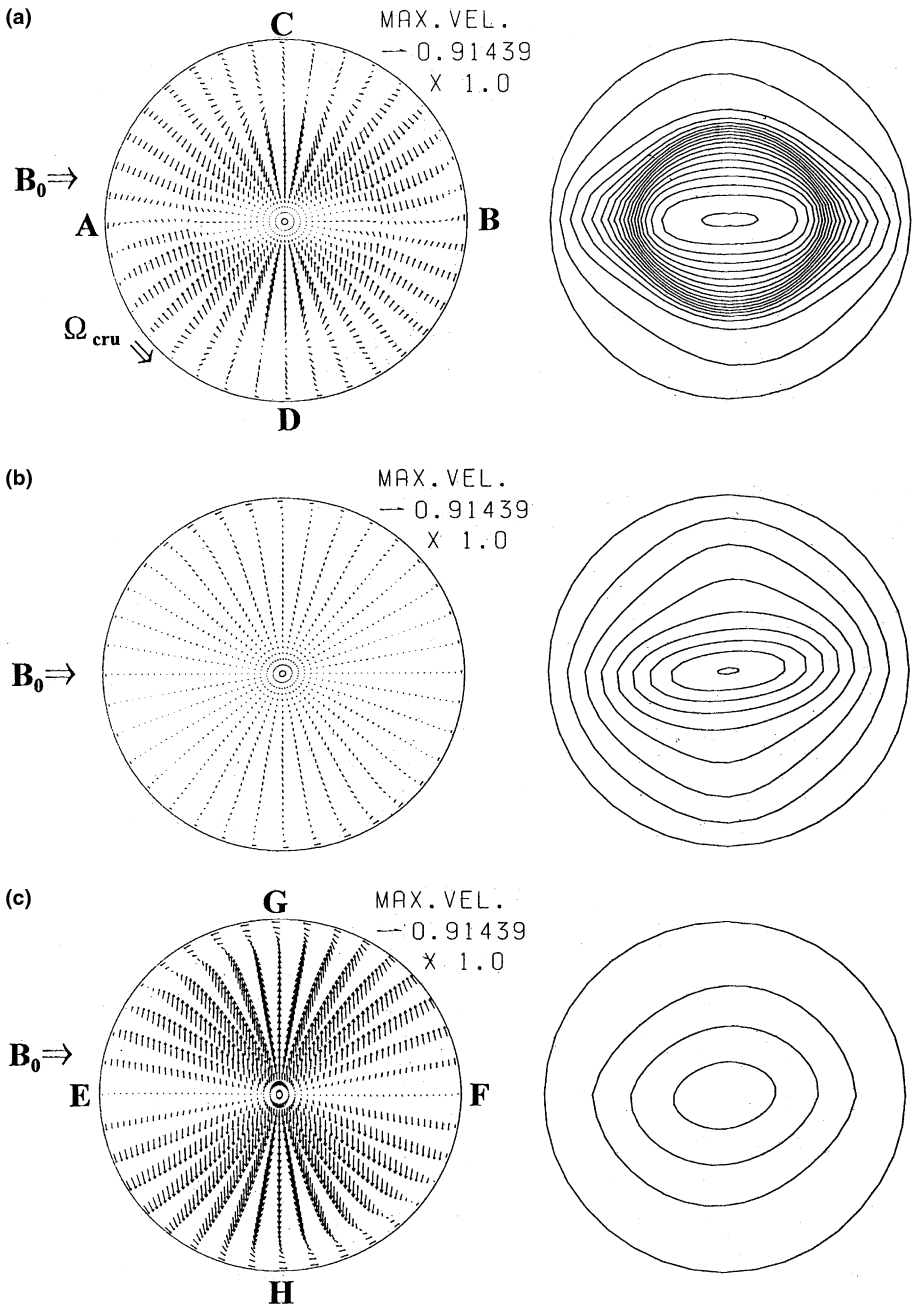

Fig. 2. Converged velocity profiles and isothermal lines in a stationary coordinate at three levels for type A ($Ha = 100$, $Ra = 2 \times 10^5$, $Pr = 0.0374$, $Re_{cry} = 0$, $Re_{cru} = -362$, $\eta = 8.09 \times 10^{-3}$): (a) $Z = 0.05H$; (b) $Z = 0.5H$; (c) $Z = 0.95H$.

for the melt surface ($= \eta$) was presumed to be 8.09×10^{-3}.

The dimensionless heat transfer rate through phase change interface, i.e., at the bottom of a crystal rod, is designated by the Nusselt number defined as follows:

$$Nu = \frac{Q_{conv}}{Q_{cond}}. \tag{12}$$

3. Computational schemes

An axial symmetric flow was not presumed in the crucible, so that fully three-dimensional results can be expected. Since staggered grid was employed, mass balance can be satisfied in each grid cell. Difficulty in solving for velocity components at a radial center could have been circumvented by the technique of Ozoe and

Toh [12]. Fluid region was divided into sub-spaces for which velocity, temperature, pressure and electromagnetic force were computed. The grid numbers to give sub-spaces were $30 \times 36 \times 40$ in the radial, in the circumferential and in the axial directions, respectively. Uniform grids were employed. The basic mathematical equations were approximated by a finite difference method. Inertial terms were approximated by a QUICK scheme [13] and the second-order central difference approximation was adopted for all other geometrical derivatives. Pressure and velocity corrections were solved with HSMAC scheme [14]. In the same way, electric scalar potential and electric current density corrections were solved by HSMAC method. Tables 1–3 show physical properties of InSb melt and furnace, numerical conditions and dimensional equivalence values, respectively.

4. Computed results

At first, transient three-dimensional numerical computations were carried out for cases $Ra = 2 \times 10^5$, $Pr = 0.0374$, $Re_{cry} = 0$, $Re_{cru} = -362$, $\eta = 8.09 \times 10^{-3}$ with a horizontal magnetic field of $Ha = 100$ (type A), 200 (type B) and 300 (type C). Model system used in these calculations is (a) model 1 with a large crystal rod at the top in Fig. 1. A steady-state convection was obtained even with transient calculation for these numerical conditions.

Fig. 2 shows converged velocity profiles and isothermal lines in a stationary coordinate at three levels: (a) $Z = 0.05H$ (near the melt surface), (b) $Z = 0.5H$ (near the middle height of the melt) and (c) $Z = 0.95H$ (near the crucible bottom) for type A ($Ha = 100$, $Ra = 2 \times 10^5$, $Pr = 0.0374$, $Re_{cry} = 0$, $Re_{cru} =$

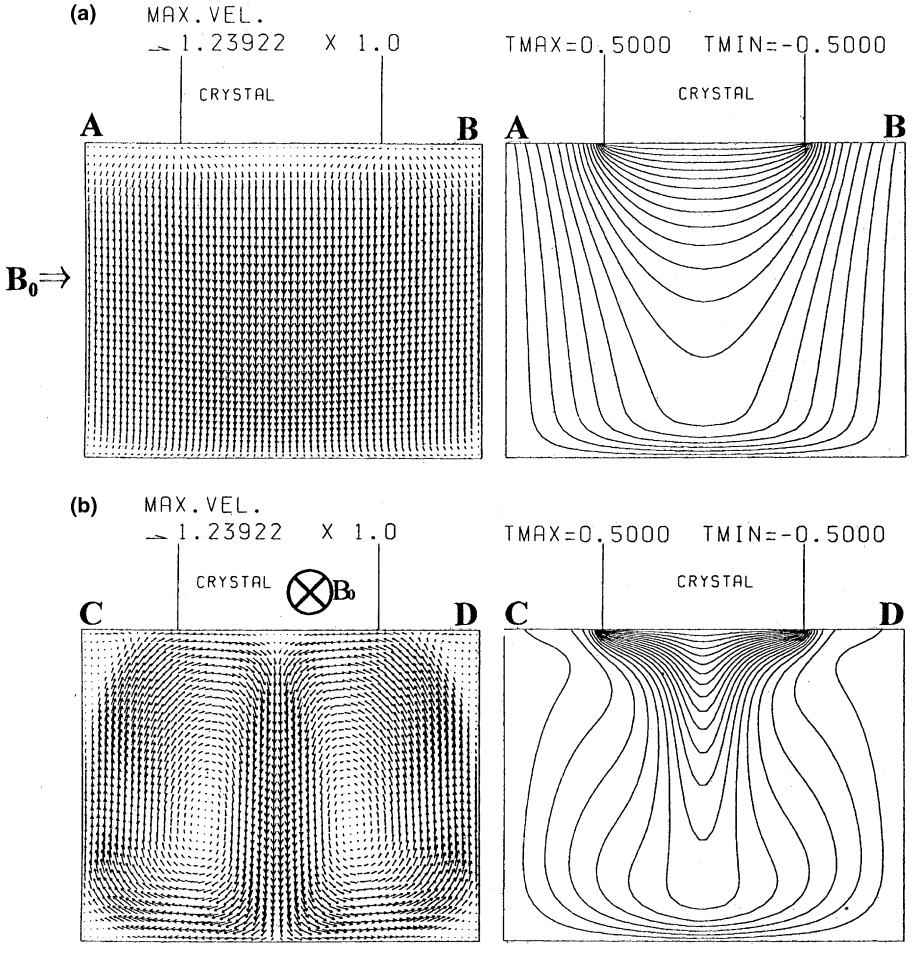

Fig. 3. Converged velocity profiles and isothermal lines for type A ($Ha = 100$, $Ra = 2 \times 10^5$, $Pr = 0.0374$, $Re_{cry} = 0$, $Re_{cru} = -362$, $\eta = 8.09 \times 10^{-3}$): (a) in a vertical cross-section at a line AB of Fig. 2(a); (b) in a vertical cross-section at a line CD of Fig. 2(a).

-362, $\eta = 8.09 \times 10^{-3}$). Rotation of a crucible is counterclockwise. In Fig. 2(a), fluid ascends from a line CD which is perpendicular to the magnetic field and descends from a line AB which is parallel to the magnetic field near the free surface. In Fig. 2(c), fluid springs from a line EF and flows to the direction of a line GH near the bottom of a crucible. The melt flow in the circumferential direction with the direction of a crucible rotation can be seen slightly along the crucible wall at all levels. Temperature contours become almost an elliptic shape. This is because fluid is cooled radiantly during the convection along the free surface and the colder fluid descends along the A–B line. Along the same radius of the melt, the fluid is colder in the A–B line than that along the C–D line. This explains the formation of elliptic isotherms. However, isothermal contour lines are tilted slightly due to the rotation of a crucible rotating counterclockwise.

Fig. 3 shows converged velocity profiles and isothermal lines in a vertical cross-section along lines, (a) A–B and (b) C–D of Fig. 2(a). In Fig. 3(a), the eminent result is that the flow in a vertical cross-section, which is parallel to the magnetic fields, is almost downward even over the heated vertical walls. On the other hand, in Fig. 3(b), strong natural convection prevailed with two roll cells in a vertical cross-section perpendicular to the magnetic field. Ascending fluid is also supplied from those descended in a cross-section at AB. Although they are not shown herein, flow patterns in horizontal and vertical cross-sections were almost identical under two different magnetic strength $Ha = 200$ (type B) and 300 (type C) for otherwise the same conditions as type A. However, with the increase in the magnetic strength, convection was more suppressed by Lorentz force. Moreover, temperature field approached to conduction condition.

Fig. 4(a)–(c) shows the converged electric field vectors **E**, the induced electromotive force vectors $\mathbf{U} \times \mathbf{B}$ and the electric current density vectors **J** in a stationary coordinate at $Z = 0.5H$ for type A. Electric current density can be calculated by the Ohm's law $\mathbf{J} = \mathbf{E} + \mathbf{U} \times \mathbf{B}$ as shown in Eq. (7). The electric field vectors **E** are produced approximately in the opposite direction of $\mathbf{U} \times \mathbf{B}$ vectors. In a horizontal cross-section, $\mathbf{U} \times \mathbf{B}$ vectors are decided only by an axial velocity **W** as shown in Eq. (9). That is, the downward flow is domi-

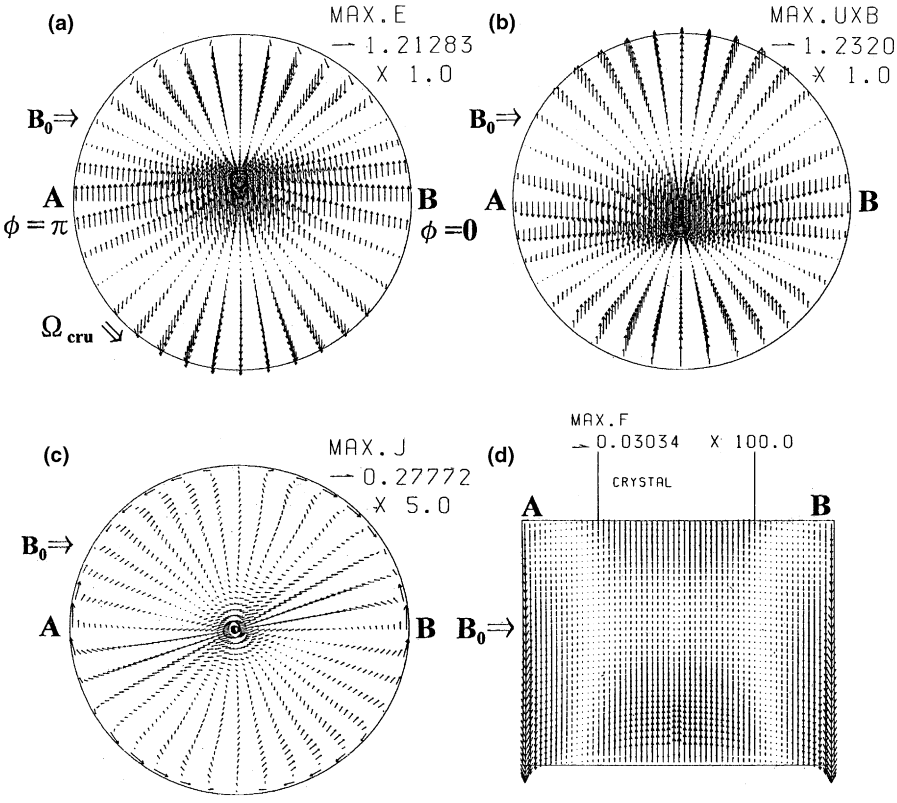

Fig. 4. The converged electrical field for type A ($Ha = 100$, $Ra = 2 \times 10^5$, $Pr = 0.0374$, $Re_{cry} = 0$, $Re_{cru} = -362$, $\eta = 8.09 \times 10^{-3}$): (a) the electric field vectors **E**; (b) the induced electromotive force vectors $\mathbf{U} \times \mathbf{B}$; (c) the electric current density vectors **J** in a stationary coordinate at $Z = 0.5H$; (d) Lorentz force vectors **F** in a vertical cross-section along a line AB.

nant near a line AB. On the other hand, the upward flow is dominant near a line CD. In Fig. 4(c), large electric current densities are produced along a crucible wall. It is considered that the electric current density is approximately decided by the electric field near the vertical crucible wall. $\mathbf{U} \times \mathbf{B}$ vectors become small near the sidewall since an axial velocity is 0 on the vertical crucible wall. The resulted $\mathbf{J}$ vectors are produced in the direction of $\mathbf{E}$ vectors. On the other hand, $\mathbf{U} \times \mathbf{B}$ vectors are produced with the almost same magnitude as $\mathbf{E}$ vectors for the inside of fluid. Therefore, $\mathbf{J}$ vectors become quite small compared with those along a crucible wall for the inside of fluid. Fig. 4(d) shows converged Lorentz force vectors $\mathbf{F}$ in a vertical cross-section along a line AB. The downward Lorentz forces are quite dominant along the vertical heated crucible wall. These forces are induced by large electric current densities along a crucible wall as seen in Fig. 4(c). These forces suppress the buoyant flow along a vertical heated crucible wall. Under a crystal rod, upward Lorentz forces are dominant which suppresses the downward natural convection from a cold crystal rod. Apparently, it is considered that these combinations of the Lorentz forces rectify the downward flow as shown in Fig. 3(a). Similar effect was computed for natural convection of liquid metal in a cube heated and cooled from vertical walls [17].

Fig. 5(a)–(c) shows the converged electric field vectors $\mathbf{E}$, the induced electromotive force vectors $\mathbf{U} \times \mathbf{B}$ and the electric current density vectors $\mathbf{J} = \mathbf{E} + \mathbf{U} \times \mathbf{B}$ in a vertical cross-section along a line AB for type A. In Fig. 5(c), large electric current densities are produced near the vertical crucible wall. These directions agree with the directions of $\mathbf{U} \times \mathbf{B}$ vectors. The induced electromotive force in the vertical cross-section, which is parallel to the magnetic field, is decided by circumferential velocity as shown in Eq. (9). Therefore, $\mathbf{J}$ vectors with the direction of $\mathbf{U} \times \mathbf{B}$ vectors along a vertical crucible wall are produced dependent on the flow in the circumferential direction with the rotational direction of a crucible. Moreover, these electric current densities induce Lorentz forces as seen in Fig. 5(d). Fig. 5(d) shows converged Lorentz force vectors $\mathbf{F}$ in a stationary coordinate at $Z = 0.5H$ for type A. The directions of the

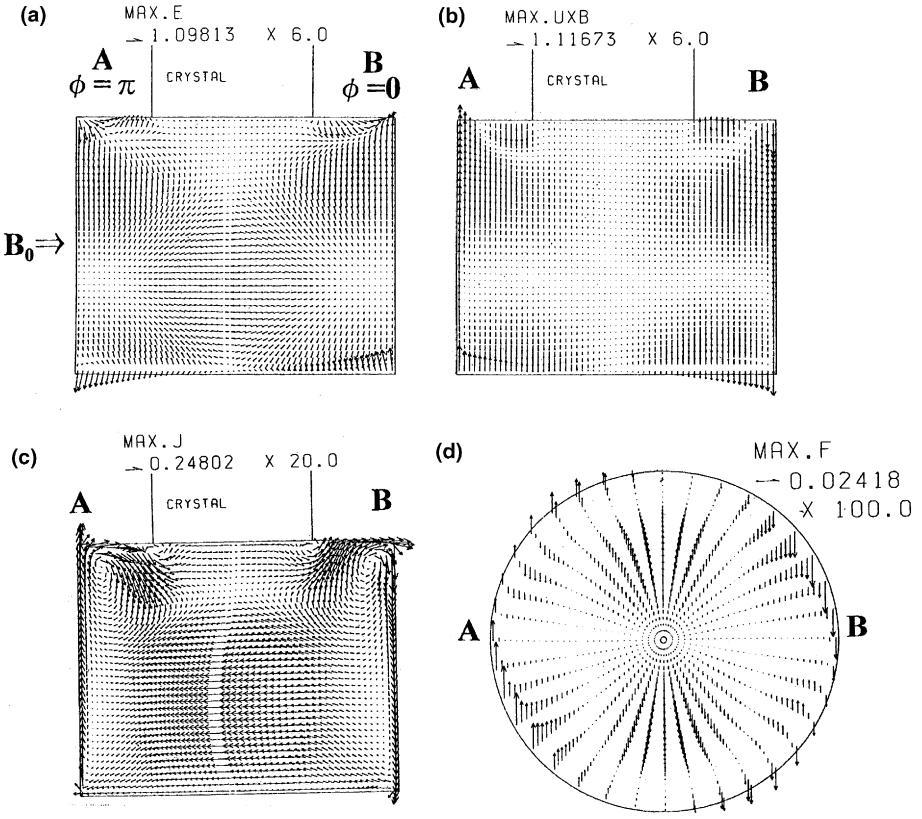

Fig. 5. The converged electrical field for type A ($Ha = 100$, $Ra = 2 \times 10^5$, $Pr = 0.0374$, $Re_{cry} = 0$, $Re_{cru} = -362$, $\eta = 8.09 \times 10^{-3}$): (a) the electric field vectors $\mathbf{E}$; (b) the induced electromotive force vectors $\mathbf{U} \times \mathbf{B}$; (c) the electric current density vectors $\mathbf{J}$ in a vertical cross-section along a line AB; (d) Lorentz force vectors $\mathbf{F}$ in a stationary coordinate at $Z = 0.5H$.

occurrence of these forces are opposite to the rotational direction of a crucible. It is considered that the isotherms become elliptic in a Czochralski system with a crucible rotation since the buoyant flow and the melt flow in the circumferential direction with the direction of a crucible rotation are suppressed by the Lorentz force and moreover the natural convection becomes dominant in a vertical cross-section perpendicular to the magnetic field. Even if the crucible rotates, the melt appears to be fixed in a space and both velocity and temperature fields become similar to those in a quiescent crucible [18].

Next, transient three-dimensional numerical computation of type D was carried out under the same conditions as type B. However, model system used in this calculation is (b) model 2 with a small crystal rod at the top in Fig. 1. A steady-state convection was obtained like types A–C.

Fig. 6(a) and (b) shows converged velocity profiles and isothermal lines in a stationary coordinate at $Z = 0.05H$ for type D ($Ha = 200$, $Ra = 2\times10^5$, $Pr = 0.0374$, $Re_{cry} = 0$, $Re_{cru} = -362$, $\eta = 8.09 \times 10^{-3}$). Rotation of a crucible is counterclockwise. In Fig. 6(a), the influence of the crucible rotation is represented quite strongly compared with the melt flow of type A as shown in Fig. 2(a). However, temperature contours become almost an elliptic shape. Fig. 6(c) and (d) shows converged velocity profiles in a vertical cross-section along lines, A–B and C–D of Fig. 6(a). Flow patterns in these vertical cross-section are the almost same as type A. However, convection in these planes is rather weak because of diminution of a phase change interface.

These two computed cases for different sizes of a crystal rod suggest that formation of elliptic shape isotherms are not affected by the size of a crystal rod but due to the horizontal magnetic field. Such elliptic isotherms have already been established even at the time of necking stage and may develop a whole growth of an elliptic cross-sectional crystal rod.

We then computed the streak lines to study the flow mode more in detail. Fig. 7 shows particle paths in a stationary coordinate for type A. Square symbols indicate starting location. Triangle symbols indicate final location. Duration of the computation of particle path is $\tau = 2000$. Picture (a) is a top view. Picture (b) is a side

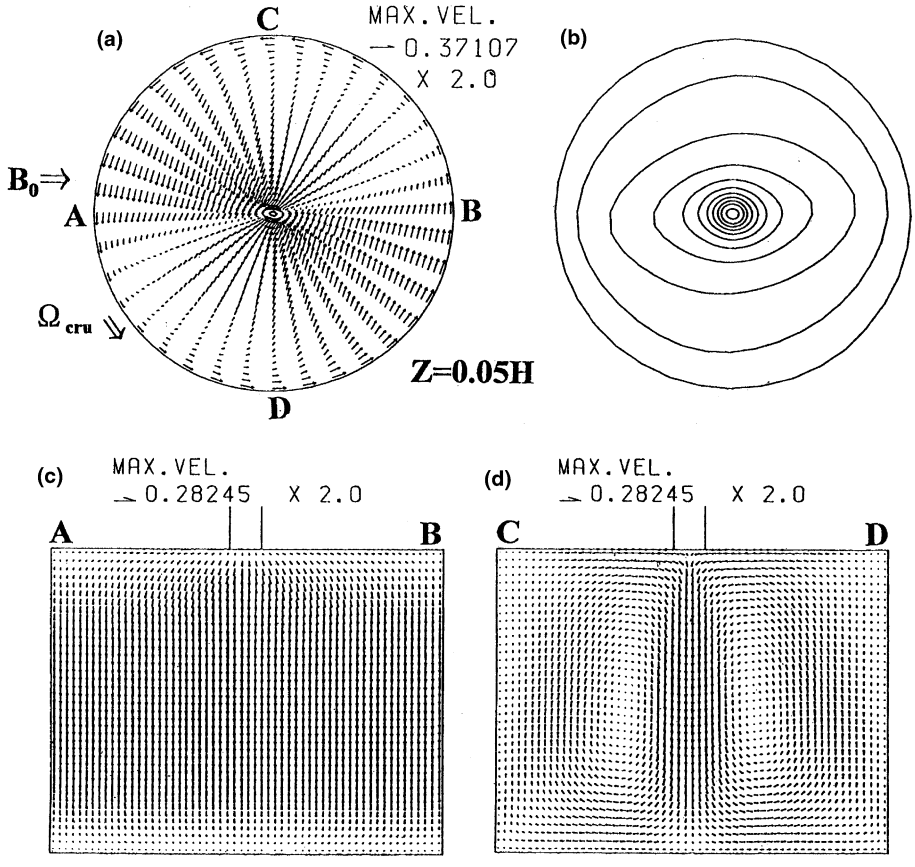

Fig. 6. Converged velocity profiles and isothermal lines for type D ($Ha = 200$, $Ra = 2 \times 10^5$, $Pr = 0.0374$, $Re_{cry} = 0$, $Re_{cru} = -362$, $\eta = 8.09 \times 10^{-3}$): (a), (b) at $Z = 0.05H$; (c) in a vertical cross-section along a line AB; (d) in a vertical cross-section along a line CD.

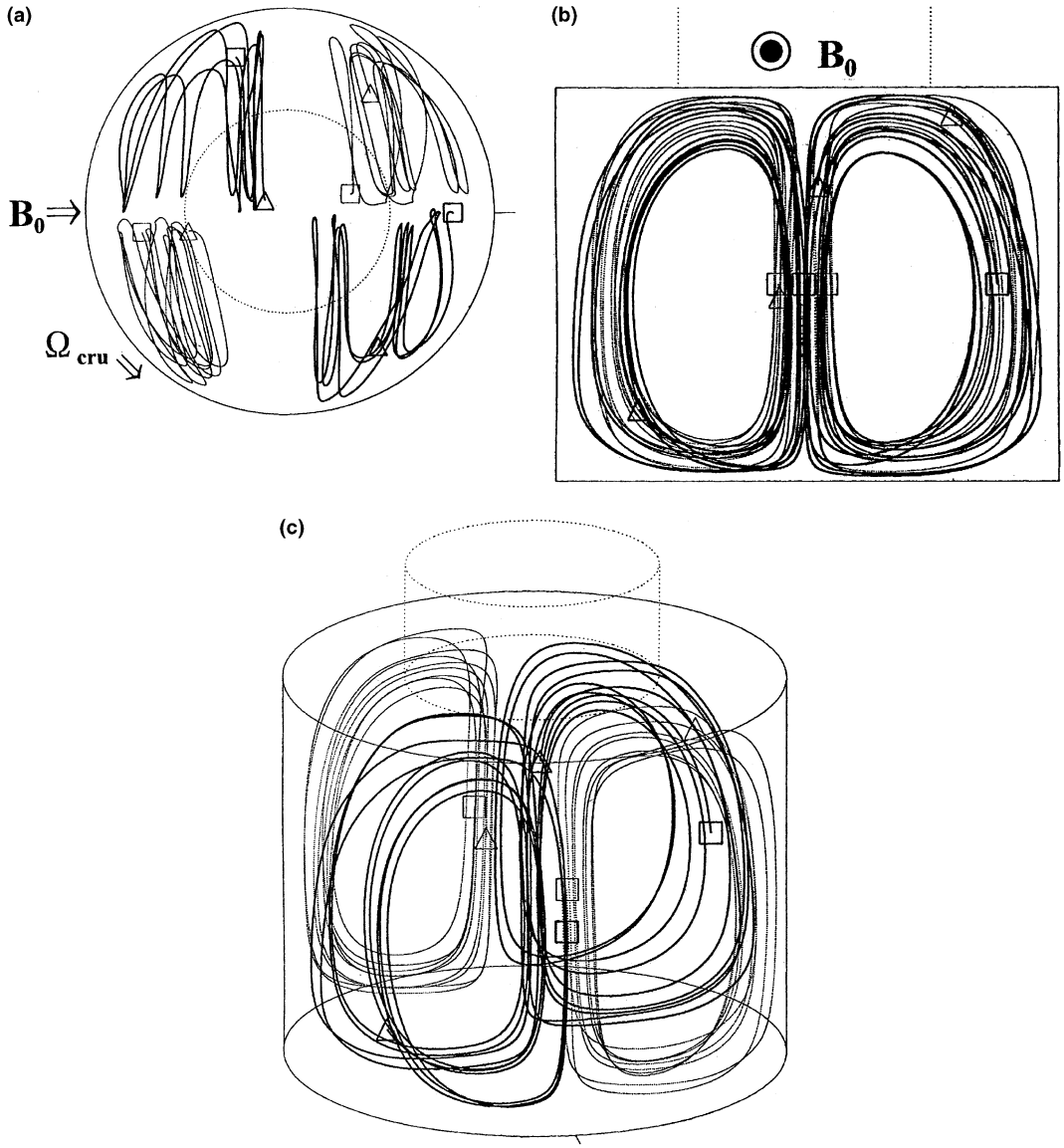

Fig. 7. Particle paths in a stationary coordinate for type A ($Ha = 100$, $Ra = 2 \times 10^5$, $Pr = 0.0374$, $Re_{cry} = 0$, $Re_{cru} = -362$, $\eta = 8.09 \times 10^{-3}$). Square symbols indicate starting location. Triangle symbols indicate final location. (a) Top view, (b) side view. (c) Perspective view of (a) and (b). Square symbols indicate starting location. Triangle symbols indicate final location.

view. Rotation of a crucible is counterclockwise. Four particles are moving in a separate area. Convection domains are separated into four regions due to a magnetic field although the particles move helically still inside each region.

Fig. 7(c) shows a perspective view of Fig. 7(a) and (b). This represents more clearly the general behavior of the present flow field.

Under a horizontal magnetic field applied for liquid-encapsulated Czochralski technique, the elliptic cross-sectional crystal rod was grown practically by Kajigaya et al. [19]. They grew a single crystal of GaAs as reproduced in Fig. 8. The conditions are $N_{cru} = 2$ rpm, $N_{rod} = 0$ rpm. Picture "a" is a top view of the ingot. Picture "b" is a side view of the ingot. The major diameter of the elliptic crystal is parallel to the direction of the magnetic field and the minor diameter is normal to the direction of the magnetic field. In this way, they grew a single crystal rod with an elliptic cross-section actually under a horizontal magnetic field which supports the present computation extensively.

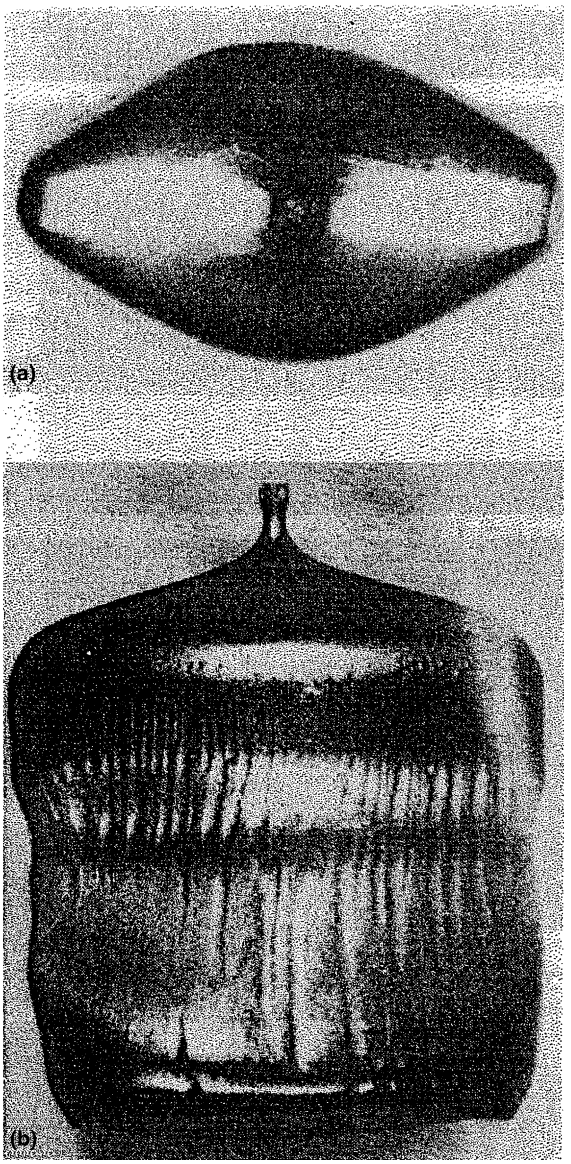

Fig. 8. The pulled ingot grown under a horizontal magnetic field applied for liquid-encapsulated Czochralski technique [19]: (a) top view of the ingot; (b) side view of the ingot.

Fig. 9 shows the effect of the Hartmann number on the volume-averaged velocity components and the averaged Nusselt number at the phase change interface for types A–D. The volume-averaged velocity components in the radial (U), in the circumferential (V), in the axial (W) directions and the average Nu number decreased monotonously with the increase in the strength of magnetic field. This means that convection was suppressed by Lorentz force. Each value of model 2 is quite small compared with that of model 1 because of diminution of a phase change interface.

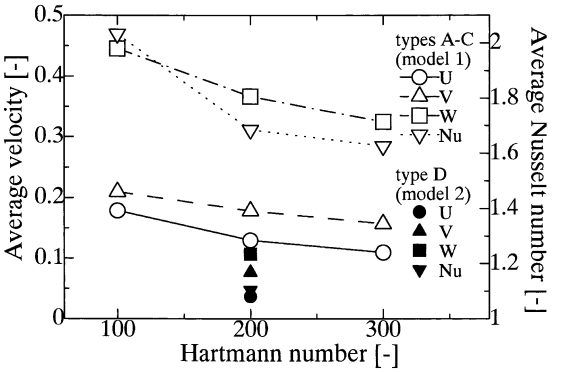

Fig. 9. Effect of the Hartmann number on the volume-averaged velocity components and the averaged Nusselt number at the phase change interface for types A–D ($Ha = 100$, 200 and 300, $Ra = 2 \times 10^5$, $Pr = 0.0374$, $Re_{cry} = 0$, $Re_{cru} = -362$, $\eta = 8.09 \times 10^{-3}$).

5. Conclusions

Transient three-dimensional numerical computations were carried out for the melt flow in a Czochralski system with a horizontal magnetic field for the two different diameters of a crystal rod with a rotating crucible. The computed velocity fields were quite peculiar. In a vertical cross-section parallel to the magnetic field all the fluid descends evenly along a vertical heated wall. On the other hand, the fluid ascends strongly along heated side walls in a vertical plane perpendicular to the magnetic field. These flows being cooled from the free surface gave elliptic shape isotherms in the melts. These results nicely explain the fore-reported elliptic cross-sectional crystal rod by Kajigaya et al. for GaAs in a horizontal magnetic field.

Acknowledgements

Fig. 8 in this paper was reprinted from Journal of Crystal Growth, vol. 112, Tomio Kajigaya, Tadashi Kimura and Yoshinori Kadota, Effect of the magnetic flux direction on LEC GaAs growth under magnetic field, pp. 123–128, Copyright (1991), with permission from Elsevier Science.

References

[1] A.F. Witt, C.J. Herman, H.C. Gatos, Czochralski-type crystal growth in transverse magnetic fields, J. Mater. Sci. 5 (1970) 822–824.

[2] K.M. Kim, Suppression of thermal convection by transverse magnetic field, J. Electrochem. Soc. 129 (1982) 427–429.

[3] H. Hirata, K. Hoshikawa, N. Inoue, Improvement of thermal symmetry in CZ silicon melts by the application of a vertical magnetic field, J. Crystal Growth 70 (1984) 330–334.
[4] H. Kohda, K. Yamada, H. Nakanishi, T. Kobayashi, J. Osaka, K. Hoshikawa, Crystal growth of completely dislocation-free and striation-free GaAs, J. Crystal Growth 71 (1985) 813–816.
[5] T. Munakata, I. Tanasawa, Onset of oscillatory flow in a Czochralski growth melt and its suppression by magnetic field, J. Crystal Growth 106 (1990) 566–576.
[6] S. Kobayashi, Effects of an external magnetic field on solute distribution in Czochralski grown crystals – a theoretical analysis, J. Crystal Growth 75 (1986) 301–308.
[7] Y. Kyung-Woo, M. Watanabe, M. Eguchi, K. Kakimoto, T. Hibiya, Change in velocity in silicon melt of the Czochralski process in a vertical magnetic field, Japan. J. Appl. Phys. 33 (1994) 487–490.
[8] K. Toh, H. Ozoe, Dopant concentration profile in a Czochralski flow of liquid metal in a vertical or a horizontal magnetic field, J. Crystal Growth 130 (1993) 645–656.
[9] H. Ozoe, M. Iwamoto, Combined effects of crucible rotation and horizontal magnetic field on dopant concentration in a Czochralski melt, J. Crystal Growth 142 (1994) 236–244.
[10] K. Kakimoto, Y. Kyung-Woo, M. Eguchi, Oxygen transfer during single silicon crystal growth in Czochralski system with vertical magnetic fields, J. Crystal Growth 163 (1996) 238–242.
[11] K. Kakimoto, Y. Kyung-Woo, Use of magnetic fields in crystal growth from semiconductor melts, Physica B 216 (1996) 406–408.
[12] H. Ozoe, K. Toh, A technique to circumvent a singularity at a radial center with application for a three-dimensional cylindrical system, Numer. Heat Transfer 33 (1998) 355–365.
[13] B.P. Leonard, A stable and accurate convective modeling procedure based on quadratic upstream interpolation, Comp. Meth. Appl. Mech. Eng. 9 (1979) 59–98.
[14] C.W. Hirt, B.D. Nichols, N.C. Romero, Technical Report, Los Alamos Science Laboratory, 1975.
[15] S. Nakamura, T. Hibiya, Thermophysical properties data on molten semiconductors, Int. J. Thermophys. 13 (1992) 1061–1083.
[16] K. Kakimoto, Numerical simulation of molten silicon flow; comparison with experiment, J. Crystal Growth 114 (1991) 715–725.
[17] T. Tagawa, H. Ozoe, Enhancement of heat transfer rate by application of a static magnetic field during natural convection of liquid metal in a cube, J. Heat Transfer 119 (1997) 265–271.
[18] M. Akamatsu, K. Kakimoto, H. Ozoe, Numerical calculation of natural and mixed convection in a Czochralski crucible under transverse magnetic fields, in: Proceeding of the 11th IHTC, vol. 3, 1998, pp. 239–244.
[19] T. Kajigaya, T. Kimura, Y. Kadota, Effect of the magnetic flux direction on LEC GaAs growth under magnetic field, J. Crystal Growth 112 (1991) 123–128.